photonics

MDPI

Article

Design and Analysis of a Photonic Crystal Fiber Sensor for Identifying the Terahertz Fingerprints of Water Pollutants

Sajjad Mortazavi [1], Somayeh Makouei [1,*], Karim Abbasian [1] and Sebelan Danishvar [2,*]

[1] Faculty of Electrical and Computer Engineering, University of Tabriz, Tabriz 51664, Iran
[2] College of Engineering, Design and Physical Sciences, Brunel University London, Uxbridge UB8 3PH, UK
* Correspondence: makouei@tabrizu.ac.ir (S.M.); sebelan.danishvar@brunel.ac.uk (S.D.)

Abstract

Ensuring the purity of water sources is a paramount global challenge, necessitating the development of highly sensitive and rapid detection technologies. In this work, a novel Zeonex-based photonic crystal fiber (PCF) sensor is designed and numerically analyzed for the effective differentiation of pure and polluted water by identifying their unique fingerprints in the terahertz (THz) spectrum. The proposed structure features a rectangular core for analyte infiltration, surrounded by a unique hybrid cladding, meticulously engineered with four inner "mode-shaping" rectangular air holes and an outer "confinement" ring of elliptical air holes. This complex topology is strategically designed to maximize the core-power fraction while ensuring robust mode confinement, enabling the exceptional performance metrics observed. The guiding properties and sensing performance of the sensor are rigorously scrutinized using the Finite Element Method (FEM) over a broad frequency range of 0.5 to 3 THz, accommodating analytes with refractive indices from 1.33 to 1.46. This range is specifically chosen to cover the refractive index of pure water (≈1.33) and a broad spectrum of common chemical and biological pollutants. The simulation results demonstrate the exceptional performance of the sensor. For polluted water, the sensor achieves an ultra-high relative sensitivity of 99.6% with a negligible confinement loss of 1.4×10^{-11} dB/m at an operating frequency of 3 THz. In contrast, pure water exhibits a high sensitivity of 96% and a confinement loss 9.4×10^{-6} of dB/m at the same frequency, showcasing a remarkable capability to distinguish between different water qualities. The superior sensitivity, extremely low loss, and structurally feasible design make the proposed PCF sensor an up-and-coming candidate for real-time water quality monitoring within the THz domain.

Keywords: photonic crystal fiber (PCF); terahertz sensor; water pollutants; effective area; confinement loss; relative sensitivity; water quality analysis

Received: 11 October 2025
Revised: 8 November 2025
Accepted: 13 November 2025
Published: 18 November 2025

Citation: Mortazavi, S.; Makouei, S.; Abbasian, K.; Danishvar, S. Design and Analysis of a Photonic Crystal Fiber Sensor for Identifying the Terahertz Fingerprints of Water Pollutants. *Photonics* **2025**, *12*, 1136. https://doi.org/10.3390/photonics12111136

1. Introduction

Water is essential for life on Earth, and it is crucial that it remains free from contaminants, safe, and clean. Both governmental and non-governmental organizations are actively promoting the consumption of clean water, while various companies are offering different methods for water purification [1,2]. The provision of safe drinking water remains one of the most pressing global challenges of the 21st century. Despite significant progress, a staggering one-quarter of the world's population, amounting to 2.1 billion people, still lacks access to safely managed drinking water, forcing hundreds of millions to rely on untreated and contaminated surface water sources [3]. This crisis is exacerbated by the

pervasive and often invisible threat of chemical contamination, particularly from heavy metals such as lead (Pb), cadmium (Cd), and arsenic (As) [4,5]. These elements are exceptionally pernicious due to their non-biodegradable nature, allowing them to persist in the environment and bioaccumulate within the food chain, where their concentrations are magnified at each trophic level [6]. The bioaccumulation of these heavy metals poses severe health risks, including neurological disorders, kidney damage, and carcinogenic effects, disproportionately affecting vulnerable populations in developing countries [7]. To combat this insidious threat, innovative detection technologies are imperative, particularly those capable of rapid, sensitive, and non-invasive identification of contaminants at trace levels [8]. In response to this pressing need, traditional analytical techniques such as atomic absorption spectroscopy, gas chromatography, and mass spectrometry have long been the gold standard for detecting water contaminants [9]. While these methods offer high precision, they are inherently limited by significant drawbacks, including complex sample preparation, reliance on bulky and expensive laboratory equipment, and lengthy processing times. These factors render them unsuitable for the real-time, and continuous monitoring required for effective public health protection and environmental management. Consequently, there is a compelling impetus to develop alternative sensing paradigms that are rapid, cost-effective, highly sensitive, and field-deployable [10–12].

Among the emerging technologies, Terahertz (THz) wave-based sensing has garnered significant attention as a powerful and non-invasive analytical tool [13]. Situated between the microwave and infrared regions of the electromagnetic spectrum (0.1–10 THz), THz radiation possesses unique properties ideal for sensing; it can penetrate many non-polar materials and, more importantly, many chemical and biological molecules exhibit distinct absorption peaks and spectral "fingerprints" in this range, enabling label-free identification [14,15]. Photonic Crystal Fibers (PCFs) have emerged as an exceptional waveguide platform to effectively guide and utilize THz waves for high-sensitivity applications [16]. The micro-structured arrangement of air holes in PCFs allows for unparalleled design flexibility and superior control over light-guiding properties, facilitating strong light-matter interaction within a hollow or porous core [17]. For THz applications, Zeonex, a cyclic olefin copolymer, stands out as an excellent background material due to its remarkably low material absorption loss, flat refractive index profile, and high chemical stability [18].

The field has witnessed numerous advancements in PCF sensor design for chemical and biological detection. Initial designs, often featuring simple hexagonal or circular lattice claddings, demonstrated the feasibility of the approach but were typically limited to moderate relative sensitivities (in the range of 50–70%) and suffered from significant confinement losses [19]. To enhance performance, subsequent research explored more intricate geometries, including porous-core structures and complex cladding arrangements, which successfully pushed sensitivities beyond 85%. However, these improvements often came at the expense of increased fabrication complexity or other compromised optical properties. A critical challenge, therefore, remains in the conception of a sensor that simultaneously achieves ultra-high sensitivity approaching unity, negligible confinement loss, and a design that remains feasible for fabrication [20].

Recent studies have increasingly emphasized the transformative potential of Terahertz photonic crystal fibers (THz-PCFs) in real-time and ultra-sensitive water quality monitoring. For instance, Kundu et al. (2025) demonstrated an optimized PCF architecture capable of detecting aquatic pathogens such as Vibrio cholerae, Escherichia coli, and Bacillus anthracis with exceptionally high sensitivities exceeding 96% at 3.2 THz, while simultaneously achieving ultra-low confinement losses on the order of 10^{-13} dB/cm. These results highlight the feasibility of THz-PCFs for pathogen-specific water surveillance under field-deployable conditions [21]. In parallel, Wang et al. (2024) developed a dual-parameter

PCF sensor employing graphene-coated microgrooves that simultaneously measures refractive index and temperature with high accuracy, thereby underscoring the versatility of THz-PCFs in multi-parameter water monitoring applications [22]. Complementary review efforts further emphasize that beyond pollutant detection, recent PCF research trends are converging toward hybrid designs that balance high sensitivity, ultra-low confinement loss, and fabrication feasibility, suggesting a clear trajectory toward practical deployment [23].

Moreover, recent reviews of THz-based water detection techniques have systematically documented the unique interaction of THz waves with liquid water, highlighting the challenges and opportunities arising from the strong absorptive nature of aqueous media [24]. Furthermore, the versatility of THz-PCF structures extends beyond direct sensing to specialized waveguiding, such as the development of ring-core fibers for transmitting orbital angular momentum (OAM) modes without phase distortion [25]. In parallel, other advanced sensing platforms, such as those combining PCF with surface plasmon resonance (SPR), have demonstrated high-sensitivity detection of parameters like magnetic field and temperature [26]. While these fields represent significant advancements, our work remains focused on the specific challenge of achieving ultra-high sensitivity specifically for aqueous analyte fingerprinting within the core, which is the focus of this work. These insights underline the necessity of carefully engineered fiber structures and material platforms, such as Zeonex and other low-loss polymers, to minimize propagation losses while maximizing the analyte-field overlap. Importantly, this growing body of work indicates that THz-PCF sensors are transitioning from theoretical design concepts to viable platforms for integrated chemical and biological water monitoring. For example, in Ref [23], multi-core and hybrid cladding structures were identified as promising future directions, enabling the simultaneous detection of chemical pollutants and microbial contaminants with unprecedented precision. Collectively, these developments reinforce the urgency and feasibility of advancing THz-PCF sensors as next-generation technologies for global water quality assurance.

To address this gap, this paper introduces a novel Zeonex-based PCF sensor meticulously designed for identifying the THz fingerprints of water pollutants. While the proposed architecture is necessarily complex (as shown in Figure 1), it features a rectangular core for analyte infiltration, strategically surrounded by a unique cladding composed of four inner rectangular air holes and an outer ring of elliptical air holes. This hybrid configuration, combining inner rectangular holes for mode-shaping and outer elliptical holes for enhanced confinement, is strategically engineered to overcome the performance limitations of simpler, conventional designs. It is precisely this intentional complexity that enables the sensor to simultaneously maximize the modal field overlap with the analyte (achieving near-unity sensitivity) and ensure robust light confinement (achieving ultra-low loss), as will be demonstrated in the subsequent sections. The subsequent sections of this paper detail the design methodology for the sensor, present a comprehensive analysis of its guiding properties, and discuss the implications of the findings.

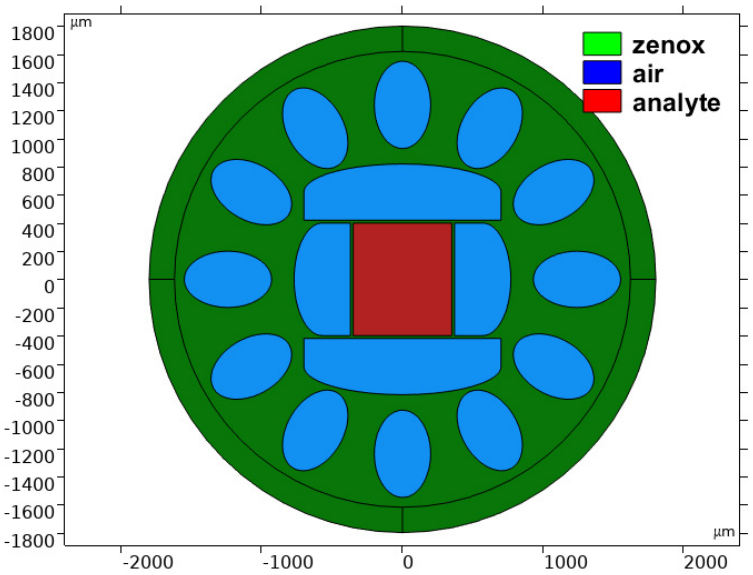

Figure 1. Two-dimensional layout of the proposed terahertz PCF sensor.

2. Sensor Design and Geometrical Structure

The performance of a PCF sensor is intrinsically linked to its geometrical configuration. In this study, a novel and highly sensitive PCF structure has been designed, the cross-sectional view of which is illustrated in Figure 1. The entire sensor architecture has been modeled and computationally analyzed using the commercial software COMSOL Multiphysics, which employs FEM to solve Maxwell's equations and accurately determine the fiber wave-guiding properties. The chosen background material for the sensor is Zeonex (a cyclic olefin copolymer), characterized by excellent properties in the THz frequency range, including a low and stable refractive index of approximately 1.53, negligible material absorption loss, and high chemical resistance—making it an ideal substrate for aqueous sensing applications. The proposed sensor architecture has been meticulously engineered to optimize the interaction between the guided THz mode and the analyte, thereby maximizing sensitivity. The design features a central rectangular core with a major axis of 800 µm and a minor axis of 700 µm. This core serves as the analyte channel, intended for infiltration with the samples under investigation—namely, pure water (with a refractive index (n) of approximately 1.33 [15,24]) and polluted water. The value of n = 1.41 was selected as a representative benchmark for heavily contaminated water. This refractive index is consistent with the presence of biological contaminants such as Giardia lamblia, as investigated in [27], and also aligns with aqueous solutions containing high concentrations of organic compounds or certain heavy metals [28,29]. This specific value (n = 1.41) thus provides a distinct and challenging benchmark to test the sensor's differentiation capability against pure water.

The core is surrounded by a sophisticated dual-ring cladding system designed to ensure robust mode confinement while enhancing light–matter interaction. The inner cladding consists of four hybrid-shaped air holes positioned symmetrically around the core: two vertically aligned structures (a rectangle of 800 µm width combined with an ellipse of 400 µm minor axis) and two horizontally aligned structures (a rectangle of 1400 µm width combined with an ellipse of 700 µm minor axis).

This asymmetric inner layer plays a crucial role in shaping the mode field and confining it tightly within the core region.

The outer cladding comprises a circular arrangement of twelve elliptical air holes, each having a major axis of 310 µm and a minor axis of 200 µm. These holes are placed at a

constant pitch (center-to-center distance) of 620 μm and are distributed with an angular separation of 30°, forming a highly symmetric and periodic barrier. This outer ring acts as a secondary confinement layer, effectively preventing THz wave leakage and significantly reducing confinement loss. To ensure accurate numerical calculation of losses, a Perfectly Matched Layer (PML) with a thickness of 10% of the fiber total diameter has been implemented at the outermost boundary to absorb radiating fields. The optimized structural parameters of the proposed PCF sensor are summarized in Table 1.

Table 1. Optimized design parameters of the proposed PCF sensor.

Parameter	Description	Value
	Core Dimensions	
Lc_major	Major axis of the rectangular core	800 μm
Lc_minor	Minor axis of the rectangular core	700 μm
	Outer Cladding	
d_major	Major axis of the elliptical air holes	310 μm
d_minor	Minor axis of the elliptical air holes	200 μm
Λ	Pitch (distance between outer ellipses)	620 μm
θ	Angular separation of outer ellipses	30°
	Inner Cladding	
W_vertical	Width of the vertical hybrid structure's rectangle	800 μm
d_vertical	Minor axis of the vertical hybrid structure's ellipse	400 μm
W_horizontal	Width of the horizontal hybrid structure's rectangle	1400 μm
d_horizontal	Minor axis of the horizontal hybrid structure's ellipse	700 μm
	Material Properties	
n_zeonex	Refractive index of the background material (Zeonex)	1.53
n_pure_water	Refractive index of pure water analyte	1.33
n_polluted_water	Refractive index of polluted water analyte	1.41

3. Numerical Formalism and Performance Metrics

To comprehensively evaluate the performance of the proposed PCF sensor, its waveguiding characteristics have been numerically investigated using FEM within the COMSOL Multiphysics software environment. This computational technique enables highly accurate analysis of electromagnetic wave propagation by discretizing the fiber cross-section into a fine triangular mesh and solving Maxwell's equations for the fundamental guided mode. A Perfectly Matched Layer (PML) boundary condition, configured with a thickness of 10% of the fiber diameter, has been implemented at the outermost boundary to emulate an open, non-reflecting space, thereby ensuring precise calculation of propagation losses. The sensor performance has been quantitatively assessed through several key parameters, including relative sensitivity, confinement loss, effective area, and numerical aperture. These figures of merit collectively provide a comprehensive understanding of the light–matter interaction, the confinement capability of the sensor, its light-gathering efficiency, and its overall potential for practical applications. The theoretical formulation of each metric is outlined below.

Relative sensitivity (R) represents one of the most critical figures of merit for a PCF-based sensor, as it directly quantifies the effectiveness of interaction between the guided light and the target analyte. A higher value of relative sensitivity indicates that a larger por-

tion of the electromagnetic field overlaps with the analyte, resulting in a more pronounced and measurable response.

It is defined as the ratio of the analyte refractive index to the real part of the effective refractive index of the guided mode, weighted by the core power fraction [30]:

$$R = \frac{n_{\text{analyte}}}{\text{Re}(n_{\text{eff}})} \times P \tag{1}$$

where n_{analyte} is the refractive index of the analyte (either pure or polluted water), and $\text{R}e(n_{\text{eff}})$ is the real part of the effective refractive index of the fundamental guided mode. The term P represents the power fraction, which is the percentage of the total optical power confined within the analyte-filled core region. This is calculated by integrating the Poynting vector (S_z) over the core area and normalizing it by the integral over the entire fiber cross-section, as given by [31]:

$$P = \frac{\int_{\text{analyte}} \text{R}\left(E_x H_y - E_y H_x\right) dxdy}{\int_{\text{total}} \text{R}\left(E_x H_y - E_y H_x\right) dxdy} \times 100 \tag{2}$$

Here E_x, H_y, E_y, H_x and are the transverse components of the electric and magnetic fields of the guided mode.

Confinement Loss (CL) is a measure of the unavoidable leakage of optical power from the core into the cladding region, which arises from the inherently imperfect confinement provided by the finite microstructure of the PCF. For a high-performance sensor, this loss must be minimized to negligible levels (ideally several orders of magnitude lower than other loss sources) to ensure a strong signal-to-noise ratio over practical fiber lengths. This parameter is directly proportional to the imaginary part of the effective refractive index and is calculated using the following standard formula [32]:

$$CL = 8.686 \times \frac{2\pi f}{c} \times \text{Im}(n_{\text{eff}}) \tag{3}$$

where f is the operating frequency in Hertz, c is the speed of light in a vacuum (3×10^8 m/s), and $\text{Im}(n_{\text{eff}})$ is the imaginary part of the effective refractive index. An extremely low value of CL is a testament to the effectiveness of the cladding design in trapping the light within the core.

The effective area (A_{eff}) characterizes the spatial extent of the guided mode intensity distribution within the fiber transverse plane. It is considered a crucial parameter for evaluating the power density and the potential for nonlinear optical effects. In the context of sensing, a smaller effective area is advantageous, as it confines the optical field more tightly, thereby enhancing the light–matter interaction. It can be expressed by the following integral relation [33]:

$$A_{eff} = \frac{\left(\iint |E(x,y)|^2 dxdy\right)^2}{\iint |E(x,y)|^4 dxdy} \tag{4}$$

where $E(x,y)$ represents the transverse electric field distribution of the fundamental mode across the entire fiber cross-section.

The Numerical Aperture (NA) is a dimensionless quantity that characterizes the range of angles over which the fiber can accept or emit light. A higher NA indicates a wider acceptance cone, which is crucial for efficiently coupling light from a source into the fiber and for collecting the transmitted signal. In the context of PCF sensors, NA is also related

to the fiber's ability to confine light. It can be determined from the effective area (A_{eff}) and operating frequency using the following relationship [34]:

$$NA = \frac{1}{\sqrt{1 + \frac{\pi A_{eff}\, f^2}{c^2}}} \tag{5}$$

where f is the operating frequency, c is the speed of light in vacuum, and A_{eff} is the effective area calculated from Equation (4). This parameter is vital for assessing the practical usability of the sensor, as it directly impacts the design and alignment tolerances of the experimental setup required for real-world measurements.

4. Numerical Result and Discussion

The performance characteristics of the proposed Zeonex-based PCF sensor have been systematically investigated across the terahertz (THz) frequency range of 0.5–3 THz. Numerical simulations, carried out using the FEM in COMSOL Multiphysics, were performed for two distinct analytes: pure water (refractive index, n_{analyte} = 1.33) and polluted water (n_{analyte} = 1.41). The numerical analysis was performed using a non-uniform, physics-controlled meshing strategy to optimize computational accuracy. The simulation domain was discretized using triangular elements with densities strategically varied according to the physical domain. A highly refined mesh was applied to the analyte-filled core, the region of primary light-matter interaction, using an 'Extremely fine' setting (maximum element size: 56 μm; minimum: 0.072 μm). The adjacent inner cladding, which is critical for mode shaping, was discretized with a 'Finer' mesh (maximum element size: 191 μm). Finally, a 'Normal' mesh (maximum element size: 241 μm) was employed for the outer cladding and PML regions, where the modal field intensity is negligible. This graduated discretization scheme was implemented to ensure maximum resolution in the critical guiding regions of the sensor.

This section provides a detailed analysis of the sensor fundamental mode-field distribution and key performance metrics—including relative sensitivity, confinement loss, effective area, and numerical aperture—to highlight the strong capability of the sensor in differentiating water quality.

The primary requirement for an effective hollow-core PCF sensor is the strong confinement of guided light within the analyte-filled core region. Figures 2 and 3 illustrate the electric-field distribution of the fundamental guided mode at the optimal operating frequency of 3 THz. Figure 2 corresponds to the pure-water analyte, whereas Figure 3 presents the results for polluted water. The two-dimensional cross-sectional views (Figures 2b and 3b) and their corresponding three-dimensional surface plots (Figures 2a and 3a) clearly demonstrate that the majority of the modal power is tightly confined within the central rectangular core for both cases.

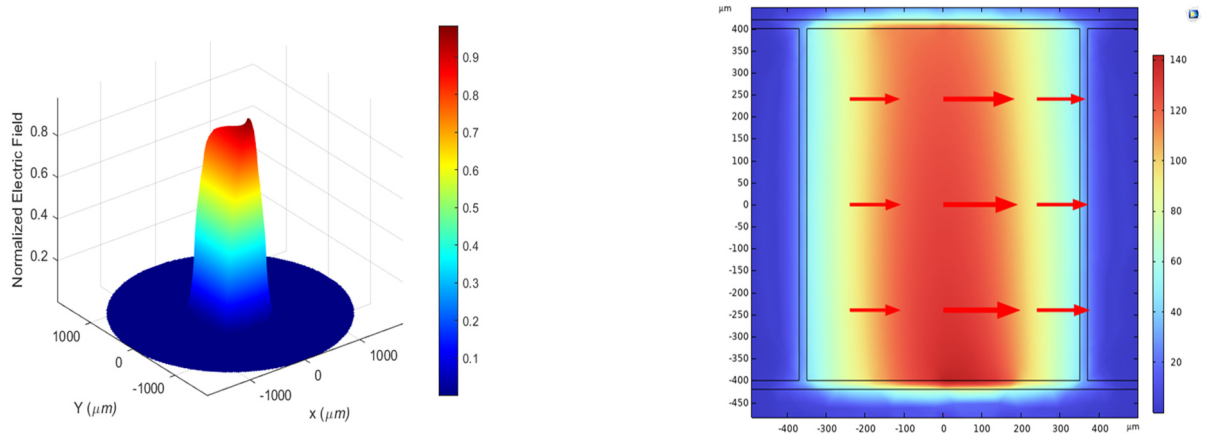

(**a**) (**b**)

Figure 2. Electric field distribution of the fundamental mode for the pure water analyte (n = 1.33) at an operating frequency of 3 THz. (**a**) 3D surface plot of the normalized electric field. (**b**) 2D cross-sectional view showing the field concentration and Poynting vector orientation within the core.

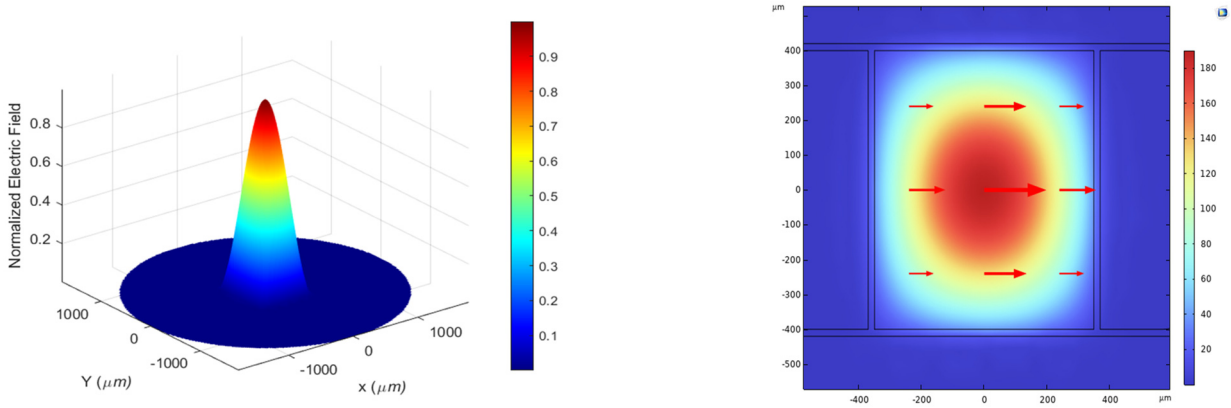

(**a**) (**b**)

Figure 3. Electric field distribution of the fundamental mode for the polluted water analyte (n = 1.41) at an operating frequency of 3 THz. (**a**) 3D surface plot. (**b**) 2D cross-sectional view.

A crucial observation is the difference in mode confinement between the two analytes. For polluted water, which has a higher refractive index, the mode field is more tightly confined within the core boundaries, as indicated by the sharper peak and narrower spatial distribution shown in Figure 3. In contrast, the mode field for pure water (Figure 2) is slightly more expanded. This phenomenon can be attributed to the smaller refractive-index contrast between the polluted-water core (n = 1.41) and the Zeonex background (n = 1.53) compared with that of the pure-water core (n = 1.33). The stronger index-guiding mechanism observed in polluted water results in a more pronounced light–matter interaction, which forms the fundamental basis for achieving higher sensitivity.

The efficiency of light–matter interaction is primarily determined by the power coupling efficiency (evaluated using Equation (2)), which is plotted as a function of frequency in Figure 4 for both pure and polluted water. The results exhibit a clear difference in behavior. For polluted water (n = 1.41), the efficiency shows a stable, monotonically increasing trend, reaching an exceptional 99.6% at 3 THz. This is due to the smaller index contrast with the background, which provides stable guiding.

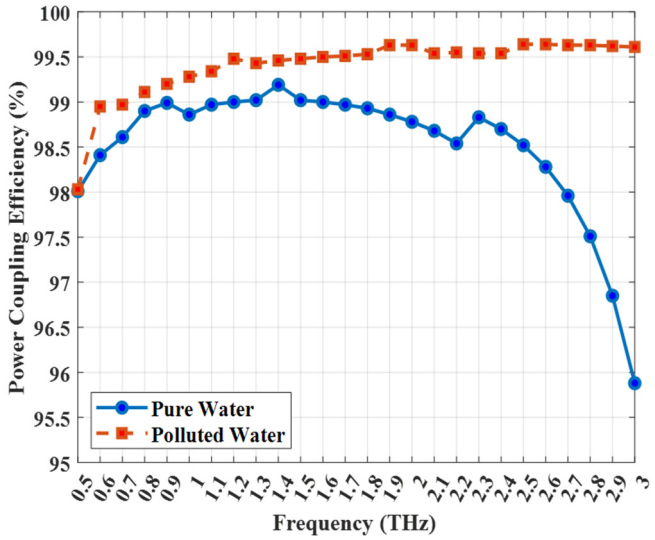

Figure 4. Power Coupling Efficiency as a function of operating frequency for pure water (n = 1.33) and polluted water (n = 1.41).

However, for pure water (n = 1.33), the efficiency peaks at approximately 1.4 THz (99.2%) before clearly decreasing. This drop is a key physical phenomenon and a known trade-off in index-guiding THz fibers. At higher frequencies, the modal field begins to contract. Due to the very large refractive index contrast between the pure water core (n = 1.33) and the high-index Zeonex background (n = 1.53), the guided mode is increasingly 'pulled' or 'squeezed' out of the low-index core and begins to propagate in the high-index Zeonex material of the cladding. This 'squeeze-out' effect reduces the core power fraction, causing the observed drop in efficiency. This effect is suppressed for the polluted water, as its higher refractive index (n = 1.41) creates a smaller, more stable index contrast with the background.

Relative sensitivity serves as the ultimate benchmark for evaluating the performance of the sensor. Figure 5 presents the calculated relative sensitivity for both pure and polluted water analytes over the frequency range of 0.5–3 THz. The graph reveals two key observations: first, the sensor achieves exceptionally high sensitivity values for both analytes; and second, there exists a distinct and significant difference in the sensitivity response between them, which is essential for effective differentiation. For polluted water (n = 1.41) the relative sensitivity increases sharply with frequency, reaching an outstanding plateau and an ultra-high value of 99.6% at 3 THz. This ultra-high value, approaching the theoretical maximum, highlights the effectiveness of the design in maximizing the light–analyte interaction and represents a substantial improvement compared with many previously reported THz PCF sensors.

For pure water (n = 1.33), the sensitivity also exhibits this trade-off, peaking at 2.3 THz (98.5%) before decreasing to 95.8% at 3 THz. The detailed physical mechanism is the same as that described for Figure 4: as the frequency surpasses 2.3 THz, the mode field contraction becomes dominant. The large index contrast (1.53 vs. 1.33) causes the mode to be 'squeezed' out of the analyte core and into the Zeonex background. This migration of the field reduces the core power fraction (P), which is a critical component of the relative sensitivity formula (Equation (1)). This reduction in core power is the dominant factor that causes the relative sensitivity to drop. In contrast, for polluted water (n = 1.41), the smaller, more stable index contrast prevents this 'squeeze-out' effect, allowing the sensitivity to maintain its high plateau.

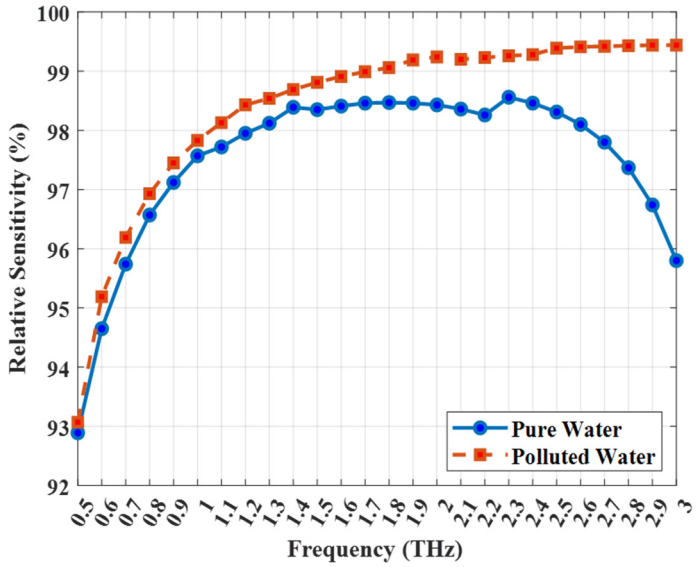

Figure 5. Relative sensitivity as a function of operating frequency for pure water (n = 1.33) and polluted water (n = 1.41).

Most importantly, the ability of the sensor to distinguish between the two water qualities is clearly demonstrated in the figure. At the optimal operating frequency of 3 THz, a significant sensitivity difference of 3.8% (99.6% for polluted water and 95.8% for pure water) is observed. This pronounced contrast, coupled with the distinct spectral profiles of the sensitivity curves, provides a unique terahertz fingerprint for each analyte. This strong differentiation capability confirms that the proposed sensor is not only highly sensitive but also highly selective, establishing it as a promising candidate for practical water-quality monitoring applications.

For any practical sensing application, the confinement loss (CL) must be minimized. CL represents the fundamental leakage of optical power from the core, which directly attenuates the signal as it propagates. While the overall signal-to-noise ratio (SNR) depends on multiple factors (including material absorption, scattering losses, and detector noise), minimizing CL is a critical design requirement. It ensures that a sufficiently strong optical signal reaches the detector, thereby maximizing the system's dynamic range and detection sensitivity over practical fiber lengths. Figure 6 presents the variation in *CL* as a function of frequency for both pure and polluted water analytes. The vertical axis is plotted on a logarithmic scale to clearly visualize the extremely low loss values obtained by the sensor, particularly at higher frequencies.

As shown in the figure, the confinement loss for both analytes exhibits a general decreasing trend with increasing frequency. This behavior is typical of index-guiding PCFs, where higher frequencies are more effectively confined within the core, resulting in an exponential reduction in power leakage through the cladding. The sophisticated dual-ring cladding structure of the proposed sensor has proven to be highly effective in this respect, reducing the confinement loss to negligible levels.

A significant distinction can be observed between the two analytes. The confinement loss for polluted water remains several orders of magnitude lower than that for pure water across the entire frequency range. This demonstrates significantly better confinement (and thus lower loss) for the analyte with the higher refractive index. For example, at 3 THz, the CL for polluted water reaches an exceptionally low value of 1.4×10^{-11} dB/m, whereas for pure water it is 9.4×10^{-9} dB/m. This difference of more than two orders of magnitude is directly associated with the stronger mode confinement in the higher-index polluted water, as discussed earlier.

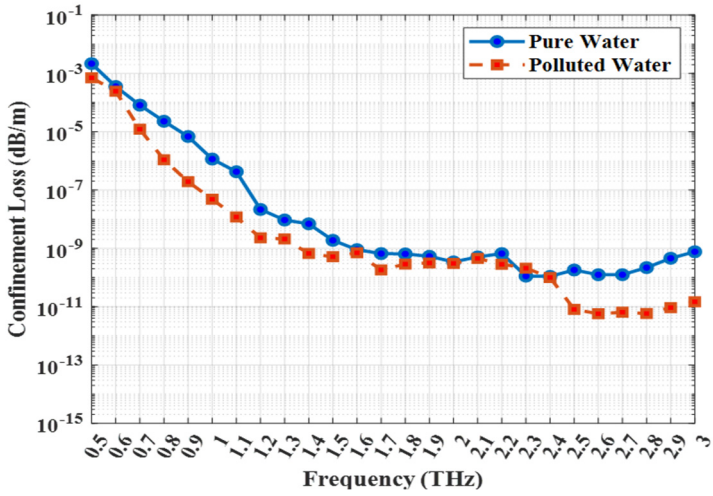

Figure 6. Confinement Loss (logarithmic scale) as a function of operating frequency for pure water (n = 1.33) and polluted water (n = 1.41).

The extremely low CL observed for polluted water enhances the practical applicability of the sensor, as it enables longer interaction lengths without significant signal degradation, thereby improving the overall detection limit. These results confirm that the proposed sensor design provides excellent light confinement—a critical prerequisite for achieving high-performance terahertz sensing.

The physical mechanisms behind the trends in Figure 6 are twofold. First, the general decrease in CL with increasing frequency is a fundamental property of index-guiding fibers. As frequency increases (and wavelength decreases), the cladding's air hole structure becomes a more effective barrier relative to the mode's wavelength, preventing the evanescent field from penetrating deeply and thus exponentially reducing power leakage. Second, the significant difference in CL between the two analytes is governed by the refractive index contrast (Δn) between the Zeonex background (n = 1.53) and the analyte core. For pure water (n = 1.33), the contrast is large ($\Delta n \approx 0.2$) while for polluted water (n = 1.41), the contrast is smaller ($\Delta n \approx 0.12$). In this guiding regime, the smaller index contrast of the polluted water results in a more stable guiding mechanism and a mode field that is more tightly bound to the core-cladding interface. This stronger binding minimizes leakage, resulting in a CL that is orders of magnitude lower than that for pure water.

The effective area (A_{eff}) provides valuable insight into the spatial distribution of the optical power and the degree of field confinement within the core. It serves as a critical parameter for assessing nonlinear optical effects and determining the efficiency of light–matter interaction in photonic crystal fiber–based sensors. A smaller effective area is generally advantageous, as it indicates tighter confinement of the electromagnetic field, thereby enhancing the overlap between the guided mode and the analyte.

Figure 7 presents the variation of (A_{eff}) with frequency for both pure and polluted water analytes. As illustrated, (A_{eff}) decreases progressively with increasing frequency, which corresponds to the stronger confinement of the THz mode at higher frequencies. This reduction is more pronounced for polluted water due to its higher refractive index, which leads to a stronger guiding mechanism and greater localization of the field within the analyte region. At 3 THz, the proposed sensor achieves (A_{eff}) = 4.9×10^7 μm^2, for polluted water and (A_{eff}) = 8.1×10^7 μm^2. for pure water. These low values confirm that the optical mode is tightly confined in the sensing core, which is highly beneficial for achieving strong light–analyte interaction. Consequently, the small effective area, combined with the extremely low confinement loss, demonstrates the ability of the sensor design to efficiently

guide and interact with terahertz waves, making it well-suited for high-sensitivity detection of water pollutants.

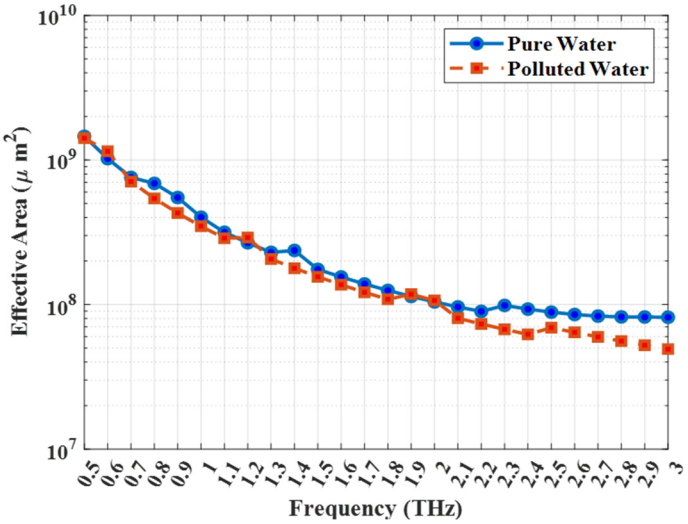

Figure 7. Effective Area (logarithmic scale) as a function of operating frequency for pure water (n = 1.33) and polluted water (n = 1.41).

The physical origins of the trends observed in Figure 7 are directly linked to the guiding mechanisms previously discussed. The decrease in A_{eff} with increasing frequency is expected, as the modal field naturally becomes more contracted and localized at higher frequencies. Furthermore, the difference in A_{eff} between the analytes confirms the confinement behavior. As established for Figure 6, the polluted water (n = 1.41) benefits from a more stable guiding mechanism due to its smaller Δn with the Zeonex background. This stronger guiding results in a modal field that is more tightly concentrated within the core boundaries, yielding a smaller effective area. Conversely, the larger Δn for pure water (n = 1.33) leads to a slightly more expanded mode (as visualized in Figure 2 compared to Figure 3), which directly corresponds to its larger A_{eff}.

To comprehensively evaluate the versatility and potential of the proposed sensor beyond water-quality monitoring, a detailed parametric analysis has been conducted by varying the analyte refractive index (n_{analyte}) from 1.33 to 1.46 with an incremental step of 0.01. This refractive-index range is of particular importance, as it covers the values corresponding to numerous environmentally relevant aqueous mixtures and pollutants, including solutions containing varying concentrations of glucose, alcohol, and a variety of industrial or agricultural chemicals. Such a range effectively represents real-world conditions in which trace contaminants or solute variations alter the refractive index of water, thereby influencing its terahertz (THz) optical response. By demonstrating stable and high performance across this entire range, the proposed sensor has proven to be highly robust and applicable as a versatile platform for diverse domains such as environmental monitoring, food-safety inspection, and chemical process control. All simulations were performed at the optimal operating frequency of 3 THz. Figure 8 presents the sensitivity as a function of the analyte refractive index. The results reveal a clear and strong positive correlation: as the refractive index of the analyte increases, the relative sensitivity of the sensor rises significantly. The sensitivity starts at approximately 96% for an analyte with n = 1.33 and rapidly exceeds 99% for analytes with n $\geq$ 1.37, asymptotically approaching the theoretical upper limit of 100%. This behavior is governed by the fundamental principle of index guiding. As the refractive index of the analyte approaches that of the Zeonex background (n = 1.53), the refractive-index contrast at the core–cladding interface is reduced,

which enhances the ability of the fiber core to confine the mode more effectively, resulting in a stronger overlap between the THz field and the analyte.

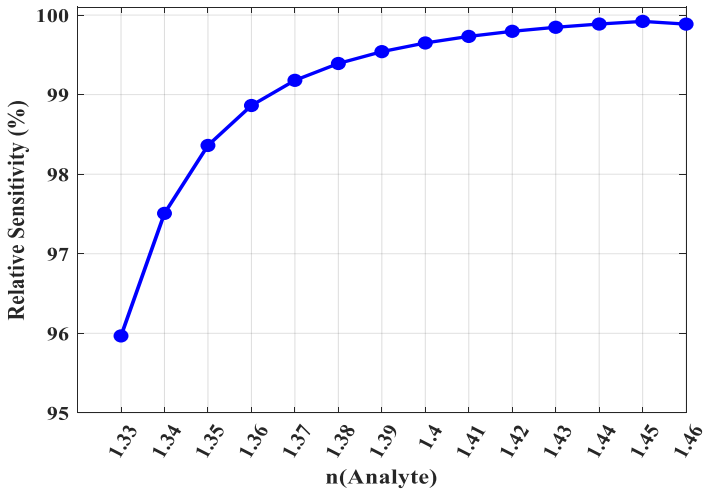

Figure 8. Relative sensitivity as a function of analyte refractive index at a fixed operating frequency of 3 THz.

To validate this interpretation, Figure 9 shows the power coupling efficiency across the same range of refractive indices. The trend observed in this graph perfectly mirrors the relative sensitivity curve confirming that higher analyte indices lead to enhanced power confinement within the core. The power coupling efficiency, which represents the percentage of light confined within the core, increases from 95.9% at n = 1.33 to an exceptional 99.8% at n = 1.46. This directly confirms that the remarkable increase in sensitivity is driven by the enhanced power confinement at higher analyte refractive indices. The near-perfect power coupling efficiency for analytes with n > 1.40 indicates that virtually the entire guided mode is interacting with the substance under test, which is the hallmark of an optimally designed sensor. This robust and predictable performance across a broad RI range makes the proposed sensor a highly reliable and powerful tool for a multitude of advanced sensing applications.

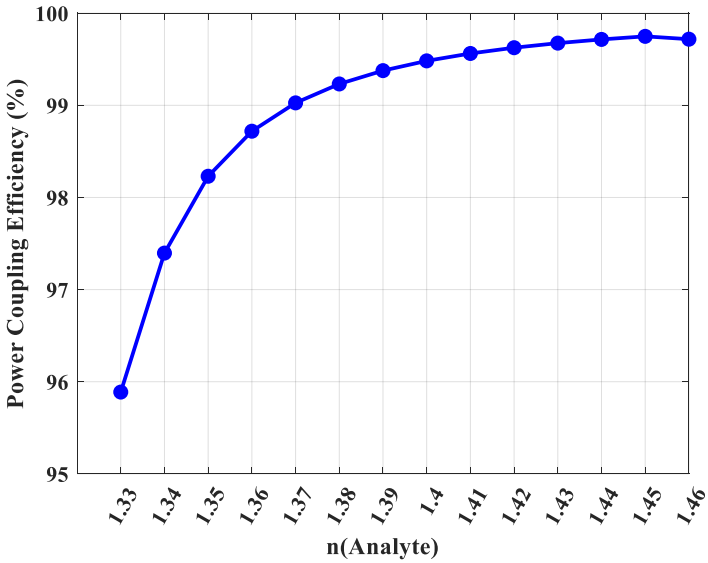

Figure 9. Power Coupling efficiency as a function of analyte refractive index at 3 THz.

Further complementing this analysis, the guiding properties of the sensor were investigated across the same refractive index range. Figure 10 plots the confinement loss as a function of the analyte's refractive index. A dramatic and highly beneficial trend is observed: the confinement loss decreases by several orders of magnitude as the analyte's refractive index increases. Specifically, the loss drops from 8.9×10^{-10} dB/m for an analyte with n = 1.33 to an exceptionally low 7.9×10^{-12} dB/m for n = 1.46. This exponential reduction is a direct testament to the enhanced mode confinement. As the analyte's refractive index approaches closer to that of the Zeonex background, the index-guiding mechanism becomes more robust, effectively creating a stronger barrier that prevents the THz wave from leaking out of the core. This characteristic is particularly advantageous, as it ensures that the sensor operates with the highest signal integrity precisely when detecting substances with higher refractive indices, which often correlate with higher concentrations or different biological materials.

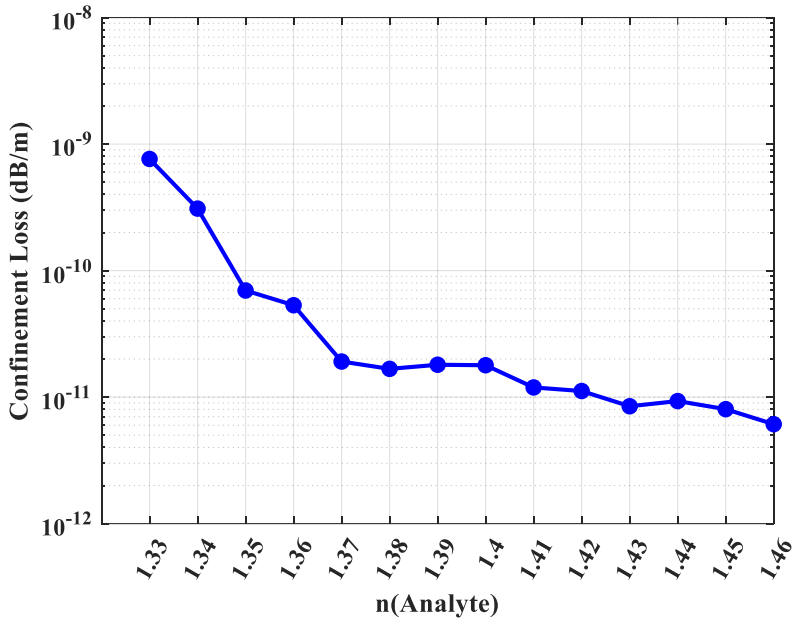

Figure 10. Confinement Loss (logarithmic scale) as a function of analyte refractive index at 3 THz.

This enhanced confinement is also reflected in the effective area (A_{eff}) and numerical aperture (NA), as shown in Figures 11 and 12, respectively. Figure 11 reveals that the effective area steadily decreases with an increasing analyte refractive index, from 8.1×10^7 μm^2 at n = 1.33 down to 4.5×10^7 μm^2 at n = 1.46. This reduction signifies that the modal power is becoming more tightly concentrated within the core for higher-index analytes, indicating a more focused mode field. This concentration of power not only contributes to the enhanced sensitivity but also confirms the stronger guiding effect. Conversely, the numerical aperture, a measure of the fiber's light-gathering capability, shows a strong positive correlation with the analyte's refractive index (Figure 12). The NA increases from 0.62 for n = 1.33 to a high value of 0.84 for n = 1.46. This is a practically significant result, as a higher NA implies a wider acceptance angle, which simplifies the process of coupling light from a THz source into the fiber. This makes the sensor more robust and tolerant to alignment variations in a real-world experimental setup, proving advantageous for efficient light coupling in practical applications. The consistent and predictable behavior of all performance metrics across this broad refractive index range firmly establishes the proposed PCF design as a versatile, reliable, and high-performance platform for a wide spectrum of THz sensing applications.

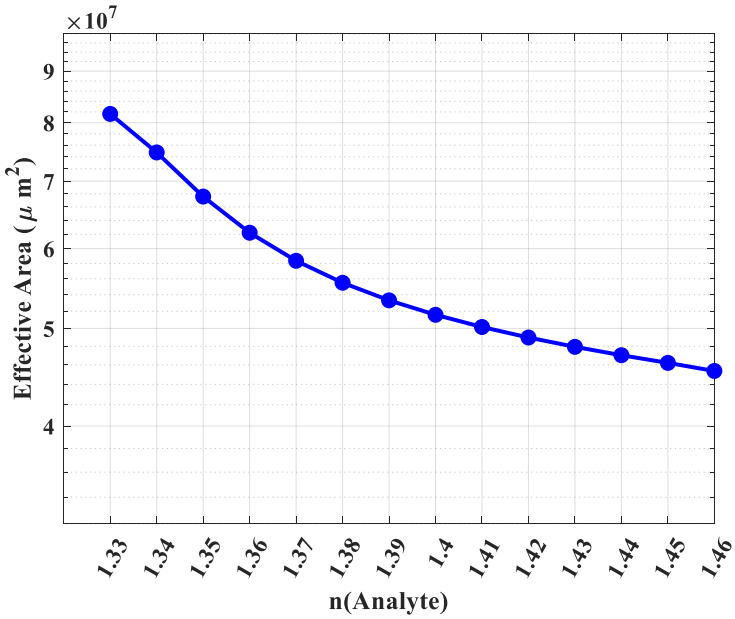

Figure 11. Effective area as a function of analyte refractive index at 3 THz.

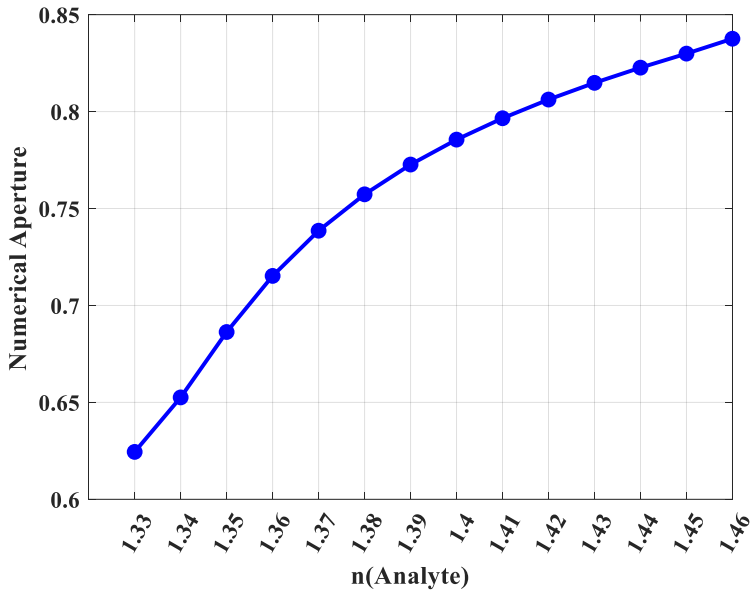

Figure 12. Numerical Aperture as a function of analyte refractive index at 3 THz.

In a practical scenario, different pollutants or varying concentrations will create a mixture with a unique, effective bulk refractive index. Our results demonstrate that the sensor is highly selective to these subtle changes. For instance, as shown in Figure 8, a small RI change from 1.39 to 1.40 results in a clear change in sensitivity. More dramatically, Figure 10 reveals that this same 0.01 RIU change induces a nearly order-of-magnitude shift in *CL* (from 1.9×10^{-11} dB/m to 1.4×10^{-11} dB/m). This high-resolution response, where small RI changes yield large, measurable changes in output parameters (especially CL), confirms the sensor's capability to differentiate between various mixtures or concentrations, thus evaluating its feasibility for practical applications. To contextualize the performance of the proposed sensor and underscore its advancements, a comparative analysis against recently published, state-of-the-art terahertz PCF sensors is presented in Table 2. The selected works represent some of the highest performing sensors in the literature for various chemical and biological sensing applications. The comparison is based on key figures of merit, including maximum relative sensitivity and minimum confinement loss.

Table 2. Performance comparison between the proposed PCF sensor and other state-of-the-art works.

Reference	Year	Core Structure	Analyte (n)	Freq. (THz)	Max. Sensitivity (%)	Min. Confinement Loss (dB/m)
Kundu et al. [21]	2025	Circular	*E. coli* (1.388)	3.2	97.54	4.41×10^{-9}
Ferdous et al. [35]	2025	Hexagonal	RBC (n = 1.65)	2	97.05	3.8×10^{-5}
Sen et al. [36]	2020	Rotated Hexagonal	Benzene (1.366)	1.0	82.26	5.84×10^{-8}
A. Habib et al. [37]	2020	Circular	Water (1.33)	2	90.7	9.54×10^{-5}
Gandhi et al. [38]	2022	Porous-core quasicrystal	Cancer cells/biological cells (n ≈ 1.37–1.40)	0.75	82.67	2.53×10^{-9}
Bulbul et al. [39]	2023	octagonal	Water (1.33)	3.6	82.46	9.9×10^{-18}
Faruk et al. [40]	2024	Hollow-core (octagonal)	Edible oil (various oils, n ≈ 1.454–1.47)	2	98.03	7.65×10^{-10}
This Work	2025	Rectangular	Polluted Water (n = 1.33–1.46)	3.0	99.6	1.40×10^{-11}

As the data in the table clearly indicates, the sensor proposed in this work stands at the forefront of current technology. With a relative sensitivity of 99.6%, it is among the highest reported values, demonstrating a near-perfect interaction between the guided mode and the analyte. Furthermore, its *CL* of 1.40×10^{-11} dB/m is exceptionally low, ensuring high signal integrity for practical applications.

5. Fabrication Tolerance Analysis

To thoroughly assess the practical feasibility and manufacturing robustness of the proposed sensor, a comprehensive fabrication tolerance analysis was conducted. In any practical fabrication process, minor dimensional deviations from the optimized design parameters are inevitable. Consequently, we systematically investigated the sensor's performance sensitivity to these potential imperfections. The analysis was performed by varying seven key structural parameters by ±1% and ±2% from their optimal values, while all other parameters were held constant. Subsequently, the sensor's relative sensitivity and confinement loss were simulated for both the polluted water analyte (n = 1.41) and the pure water analyte (n = 1.33) across the operational frequency spectrum (3 THz). The results of this comprehensive investigation are presented in Figures 13–19.

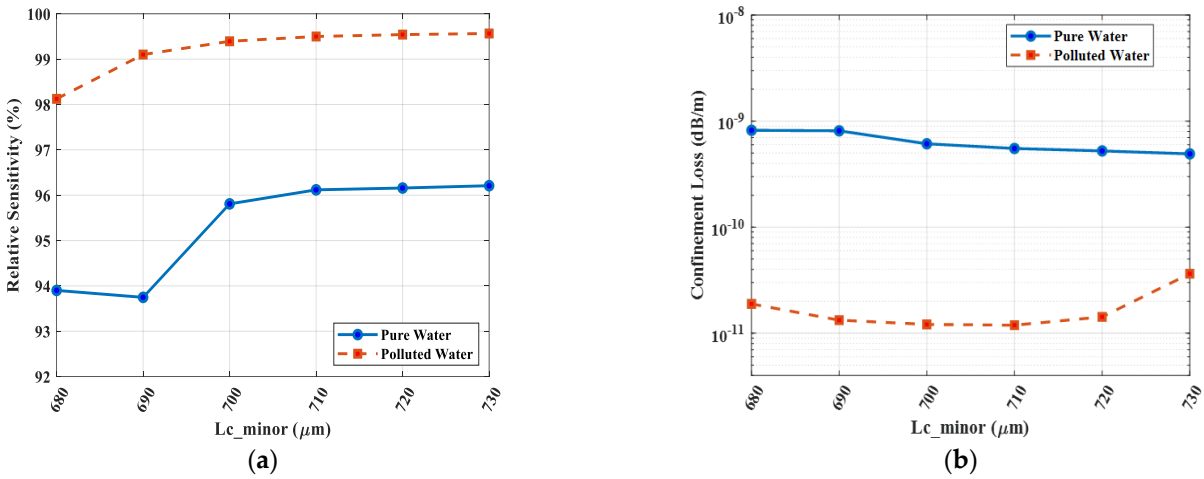

Figure 13. Fabrication tolerance analysis for (**a**) relative sensitivity and (**b**) confinement loss, showing the effect of ±1% and ±2% variations in the core minor axis (L_{c_minor}).

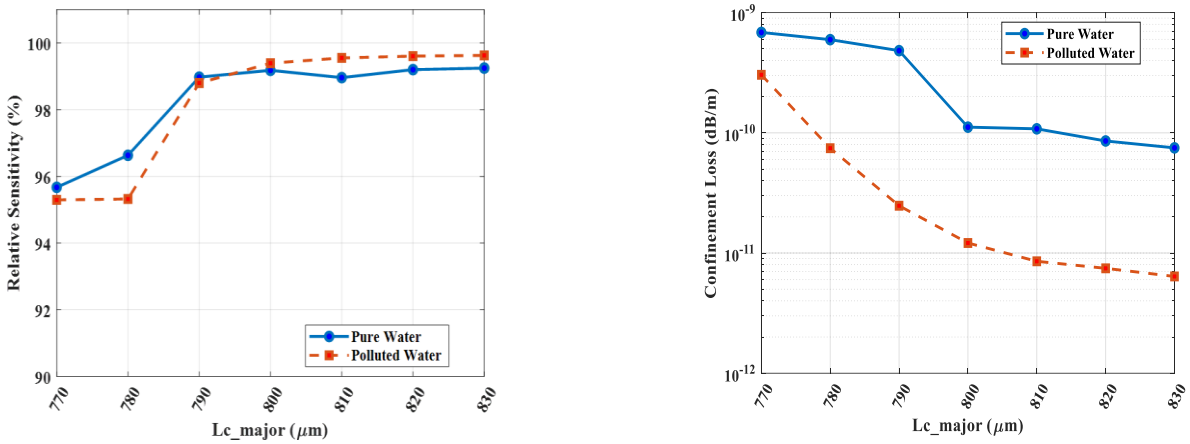

(**a**) (**b**)

Figure 14. Fabrication tolerance analysis for (**a**) relative sensitivity and (**b**) confinement loss, showing the effect of ±1% and ±2% variations in the core major axis (L_{c_major}).

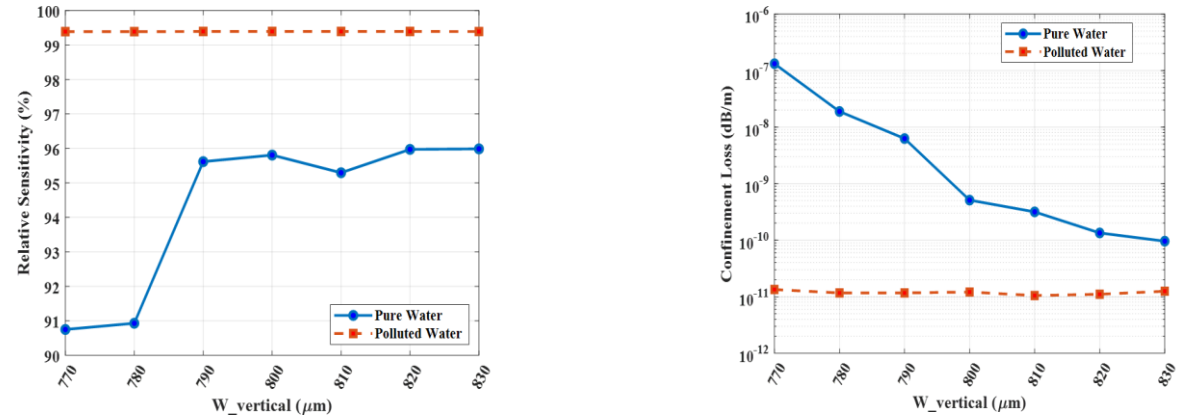

(**a**) (**b**)

Figure 15. Fabrication tolerance analysis for (**a**) relative sensitivity and (**b**) confinement loss, showing the effect of ±1% and ±2% variations in the inner cladding vertical width ($W_{vertical}$).

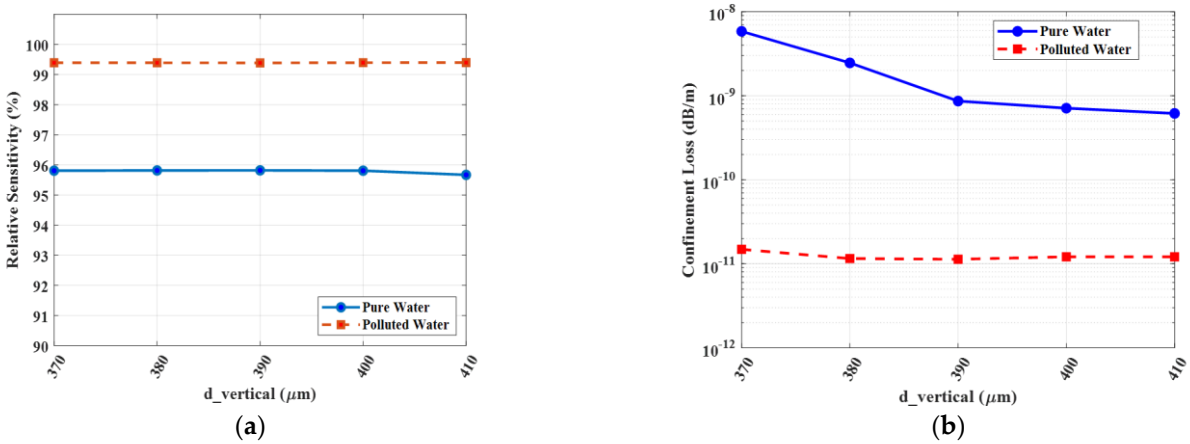

(**a**) (**b**)

Figure 16. Fabrication tolerance analysis for (**a**) relative sensitivity and (**b**) confinement loss, showing the effect of ±1% and ±2% variations in the inner cladding vertical width ($d_{vertical}$).

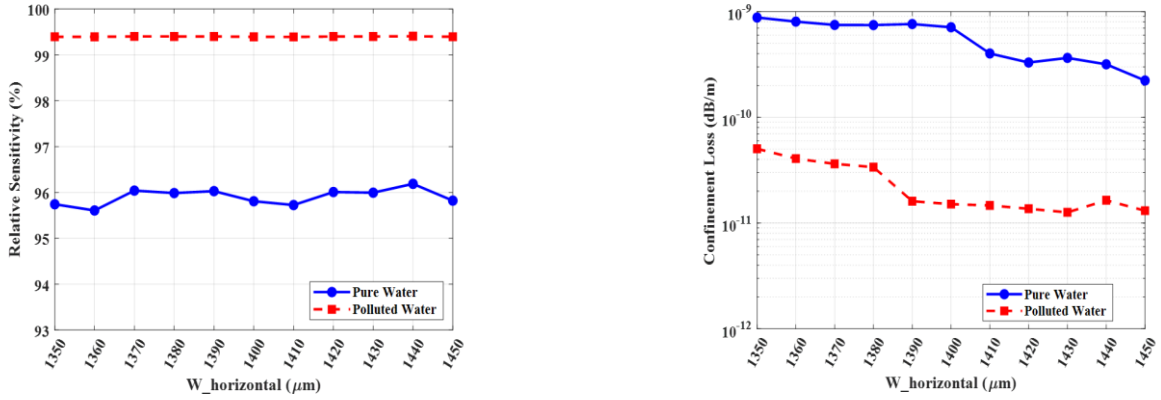

(**a**) (**b**)

Figure 17. Fabrication tolerance analysis for (**a**) relative sensitivity and (**b**) confinement loss, showing the effect of ±1% and ±2% variations in the inner cladding vertical width ($W_{horizontal}$).

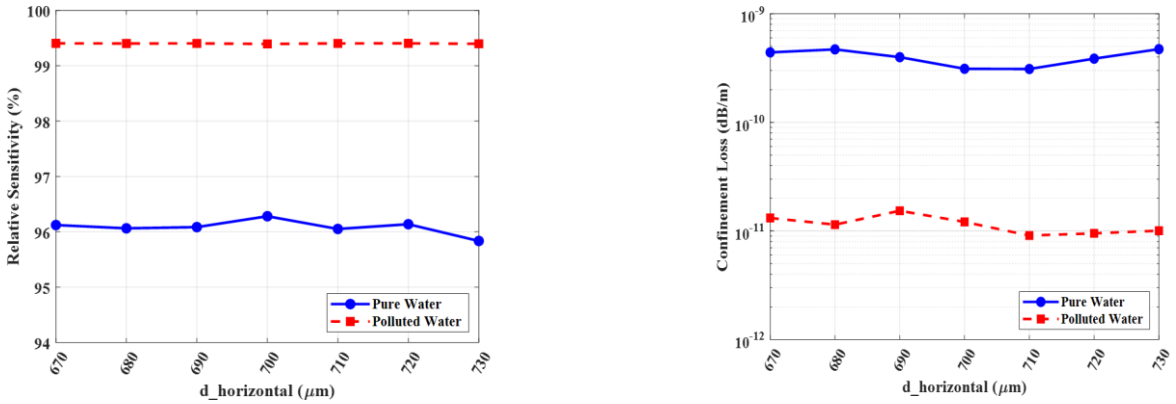

(**a**) (**b**)

Figure 18. Fabrication tolerance analysis for (**a**) relative sensitivity and (**b**) confinement loss, showing the effect of ±1% and ±2% variations in the inner cladding vertical width ($d_{horizontal}$).

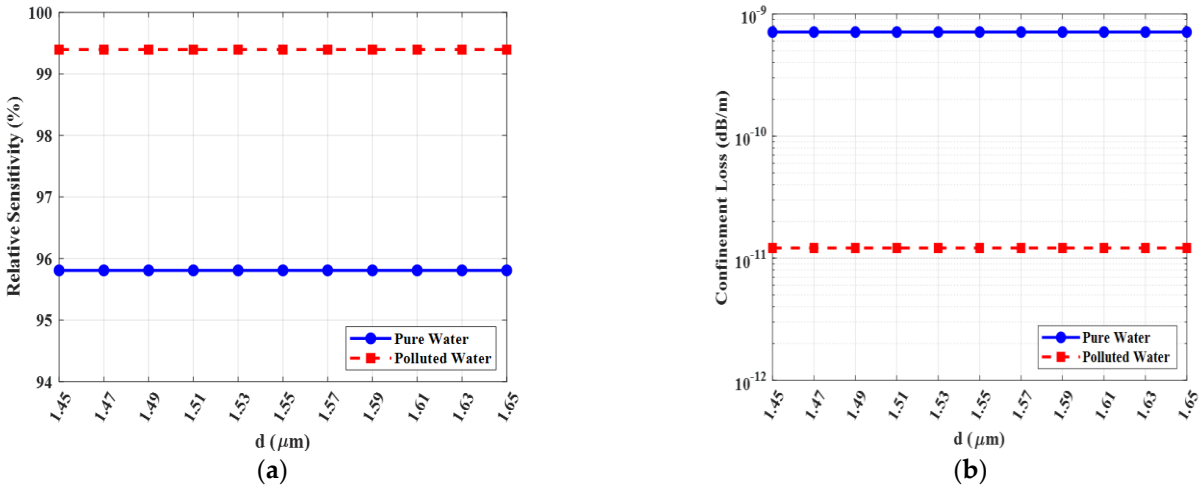

(**a**) (**b**)

Figure 19. Fabrication tolerance analysis for (**a**) relative sensitivity and (**b**) confinement loss, showing the effect of varying the outer cladding ellipticity ratio ($d = d_{major}/d_{minor}$).

A detailed examination of Figures 13–19 reveals the exceptional structural integrity of the proposed design. For both pure and polluted analytes, the performance curves corresponding to the ±1% and ±2% deviations are shown to be tightly clustered around their respective optimal design curves. This demonstrates that the sensor's high-performance

characteristics are not a critical function of achieving perfect, idealized dimensions, but rather an intrinsic property of the chosen topology.

The core dimensions (L_{c_major} =800 µm and L_{c_minor} = 700 µm) were determined through an iterative optimization process to achieve a maximized core power fraction, which simultaneously yields the highest relative sensitivity and the lowest confinement loss. Figures 13 and 14 now validate the stability of this optimum choice.

As depicted in Figures 13a and 14a for the polluted water analyte (n = 1.41), the relative sensitivity curves for ±1% and ±2% variations are tightly clustered around the optimal 99.6% value at 3 THz. For instance, a ±2% change in the core minor axis (L_{c_minor}) results in a sensitivity fluctuation of less than 0.03%, a negligible deviation. More importantly, Figures 13b and 14b demonstrate that while confinement loss is highly sensitive to the core geometry, the optimal 800 × 700 µm configuration operates at a distinct minimum (1.4×10^{-11} dB/m). Any deviation from these optimal dimensions, even by 1–2%, causes the loss to increase.

A focused analysis of the inner cladding's hybrid structures provides critical insight into the sensor's optimization. The vertical structures, defined by $W_{vertical}$ = 800 µm and $d_{vertical}$ = 400 µm, serve a dual purpose: they shape the modal field vertically while maintaining a precise distance from the core. The tolerance analysis in Figures 15 and 16 confirms the stability of this choice. As shown, these parameters operate in a stable, low-loss region for both pure (n = 1.33) and polluted (n = 1.41) analytes. Any deviation, such as a decrease in these widths, would bring the low-index air holes closer to the core, which could disrupt the mode field and compromise modal confinement, leading to higher losses. The tight clustering of the performance curves confirms that the optimal values are robust against manufacturing variations.

Similarly, the horizontal structures, defined by $W_{horizontal}$ = 1400 µm and $d_{horizontal}$ = 700 µm, are optimized to provide a wide barrier that prevents lateral mode leakage. Figures 17 and 18 validate this optimization, demonstrating that these values are centered in a stable region of minimized confinement loss. A decrease in $W_{horizontal}$, for example, would thin this barrier, creating a potential leakage path and increasing loss. Conversely, a significant increase would alter the mode shape and reduce the effectiveness of the inner barrier. Thus, the selected values are confirmed as the optimal choice, maintaining a stable, low-loss performance even when subjected to manufacturing tolerances.

Figure 19 presents the tolerance analysis for the ellipticity of the outer cladding holes, defined by the aspect ratio $d = d_{major}/d_{minor}$. The results are highly significant as they demonstrate an exceptional level of structural robustness. As shown in Figure 19a, the relative sensitivity for both pure (n = 1.33) and polluted (n = 1.41) analytes remains perfectly constant across the entire simulated range of d (1.45 to 1.65). Similarly, Figure 19b reveals that the confinement loss is also remarkably insensitive to this parameter, maintaining a stable, ultra-low value (e.g., $\approx 1.2 \times 10^{-11}$ dB/m for polluted water) across the same range. This analysis confirms that the sensor's performance is not dependent on a critically precise ellipticity. Our chosen optimal value of $d = 1.55$ (310 µm/200 µm) is therefore validated not as a narrow optimum, but as a robust setpoint located in the center of a wide, high-performance operational plateau. This insensitivity is a significant practical advantage, as it relaxes the manufacturing tolerances required for the outer cladding, further strengthening the sensor's feasibility.

6. Conclusions

In this study, a novel Zeonex-based photonic crystal fiber (PCF) sensor has been designed and comprehensively analyzed for highly sensitive detection of analytes in the terahertz (THz) frequency domain. The proposed structure, featuring a rectangular core

and a distinctive dual-ring hybrid cladding, was meticulously optimized and evaluated using the Finite Element Method (FEM). The primary objective was to develop a sensor capable of not only distinguishing between pure and polluted water but also maintaining robust performance across a broad spectrum of chemical and environmental analytes.

The numerical findings confirm the outstanding performance of the proposed design. For polluted water (n = 1.41), the sensor achieves an ultra-high relative sensitivity of 99.6%, combined with a negligible confinement loss of 1.40×10^{-11} dB/m at an operating frequency of 3 THz. This near-unity sensitivity results from the exceptional ability of the design to confine the modal field within the analyte region, ensuring maximal light–matter interaction. Furthermore, the sensor has demonstrated versatility and robustness through a comprehensive parametric analysis over a refractive-index range from 1.33 to 1.46, consistently exhibiting high sensitivity and stable guiding characteristics.

The combination of ultra-high sensitivity, extremely low *CL*, and favorable guiding properties—such as a high numerical aperture for efficient light coupling—together with a structurally feasible design, positions the proposed PCF sensor at the forefront of current state-of-the-art THz sensing technologies. When benchmarked against existing designs, the proposed configuration offers highly competitive and, in many aspects, superior performance. Overall, this work represents a significant advancement in the development of THz sensing platforms, providing a powerful and adaptable foundation for diverse applications, including real-time environmental monitoring, early-stage medical diagnostics, and food-quality assurance. Regarding practical fabrication, the proposed Zeonex-based structure, while intricate, is feasible with modern manufacturing techniques. Methods such as 3D printing (additive manufacturing), advanced extrusion, or injection molding are well-suited for creating complex polymer-based PCF structures. The rectangular core and hybrid-shaped air holes could be achieved using these high-resolution methods. While this simulation study assumes ideal smooth surfaces, we acknowledge that practical fabrication will introduce factors such as surface roughness, which is known to increase scattering losses. However, given the strong confinement of our design (as demonstrated by the ultra-low CL) and the long wavelengths of the THz regime, the impact of nanoscale surface roughness is expected to be minimal compared to the material absorption loss (which is already very low for Zeonex). Therefore, the sensor's fundamental sensitivity performance is expected to remain largely unaffected. Future work will focus on the experimental fabrication and validation of this promising design.

Author Contributions: S.M. (Sajjad Mortazavi) conducted the literature search and drafted the initial manuscript. S.M. (Somayeh Makouei), supervisor, reviewed and revised the manuscript critically for intellectual content. K.A. and S.D., writing–review and editing. All authors have read and agreed to the published version of the manuscript.

Funding: This research received no external funding.

Data Availability Statement: No data was used in this research.

Conflicts of Interest: The authors declare that there is no conflict of interest in the present study.

References

1. Shah, A.; Arjunan, A.; Baroutaji, A.; Zakharova, J. A review of physicochemical and biological contaminants in drinking water and their impacts on human health. *Water Sci. Eng.* **2023**, *16*, 333–344. [CrossRef]
2. Okafor, C.O.; Ude, U.I.; Okoh, F.N.; Eromonsele, B.O. Safe drinking water: The need and challenges in developing countries. In *Water Quality-New Perspectives*; IntechOpen: London, UK, 2024.
3. Amrose, S.E.; Cherukumilli, K.; Wright, N.C. Chemical contamination of drinking water in resource-constrained settings: Global prevalence and piloted mitigation strategies. *Annu. Rev. Environ. Resour.* **2020**, *45*, 195–226. [CrossRef]

4. Idris, M.G.; Umaru, D.; Aliyu, A.N.; Musa, I.H. Atomic absorption spectroscopy analysis of heavy metals in water at Daura gypsum mining site, Yobe state, Nigeria. *J. Found. Appl. Phys.* **2022**, *8*, 227–234.
5. Fu, Z.; Xi, S. The effects of heavy metals on human metabolism. *Toxicol. Mech. Methods* **2020**, *30*, 167–176. [CrossRef] [PubMed]
6. Ilyas, K.; Iqbal, H.; Akash, M.S.H.; Rehman, K.; Hussain, A. Heavy metal exposure and metabolomics analysis: An emerging frontier in environmental health. *Environ. Sci. Pollut. Res.* **2024**, *31*, 37963–37987. [CrossRef]
7. Edo, G.I.; Samuel, P.O.; Oloni, G.O.; Ezekiel, G.O.; Ikpekoro, V.O.; Obasohan, P.; Ongulu, J.; Otunuya, C.F.; Opiti, A.R.; Aiakaye, R.S.; et al. Environmental persistence, bioaccumulation, and ecotoxicology of heavy metals. *Chem. Ecol.* **2024**, *40*, 322–349. [CrossRef]
8. Meher, A.K.; Zarouri, A. Environmental applications of mass spectrometry for emerging contaminants. *Molecules* **2025**, *30*, 364. [CrossRef]
9. Okoffo, E.D.; Thomas, K.V. Quantitative analysis of nanoplastics in environmental and potable waters by pyrolysis-gas chromatography–mass spectrometry. *J. Hazard. Mater.* **2024**, *464*, 133013. [CrossRef]
10. Ateia, M.; Wei, H.; Andreescu, S. Sensors for emerging water contaminants: Overcoming roadblocks to innovation. *Environ. Sci. Technol.* **2024**, *58*, 2636–2651. [CrossRef]
11. Ferrari, A.G.M.; Crapnell, R.D.; Banks, C.E. Electroanalytical overview: Electrochemical sensing platforms for food and drink safety. *Biosensors* **2021**, *11*, 291. [CrossRef]
12. Wlodkowic, D.; Karpiński, T.M. Live-cell systems in real-time biomonitoring of water pollution: Practical considerations and future perspectives. *Sensors* **2021**, *21*, 7028. [CrossRef]
13. Movsisyan, M.; Al-Rossais, A.A.; Sayeed, S.; Movsisyan, G. Applications of terahertz waves in medical diagnostics: A literature review. *Int. J. Community Med. Public Health* **2024**, *11*, 2450. [CrossRef]
14. Rahman, A.; Khaleque, A.; Ali, M.Y.; Rahman, M.T. THz spectroscopic sensing of liquid chemicals using a photonic crystal fiber. *OSA Contin.* **2020**, *3*, 2982–2996. [CrossRef]
15. Ge, H.; Sun, Z.; Jiang, Y.; Wu, X.; Jia, Z.; Cui, G.; Zhang, Y. Recent advances in THz detection of water. *Int. J. Mol. Sci.* **2023**, *24*, 10936. [CrossRef]
16. Chaudhary, V.S.; Kumar, D.; Pandey, B.P.; Kumar, S. Advances in photonic crystal fiber-based sensor for detection of physical and biochemical parameters—A review. *IEEE Sens. J.* **2022**, *23*, 1012–1023. [CrossRef]
17. Mortazavi, S.; Makouei, S.; Abbasian, K.; Danishvar, S. Exhaled Breath Analysis (EBA): A Comprehensive Review of Non-Invasive Diagnostic Techniques for Disease Detection. *Photonics* **2025**, *12*, 848. [CrossRef]
18. Islam, M.S.; Sultana, J.; Rifat, A.A.; Dinovitser, A.; Ng, B.W.H.; Abbott, D. Terahertz sensing in a hollow core photonic crystal fiber. *IEEE Sens. J.* **2018**, *18*, 4073–4080. [CrossRef]
19. Kaur, V.; Singh, S. Design approach of solid-core photonic crystal fiber sensor with sensing ring for blood component detection. *J. Nanophotonics* **2019**, *13*, 026011. [CrossRef]
20. Eid, M.M.; Habib, M.A.; Anower, M.S.; Rashed, A.N.Z. Highly sensitive nonlinear photonic crystal fiber based sensor for chemical sensing applications. *Microsyst. Technol.* **2021**, *27*, 1007–1014. [CrossRef]
21. Kundu, D.; Badhon, N.U.; Ferdous, A.I.; Islam, M.S.; Hasan, M.G.; Noor, K.S.; Bani, M.M. Optimized PCF architectures for THz detection of aquatic pathogens: Enhancing water quality monitoring. *PLoS ONE* **2025**, *20*, e0317533. [CrossRef]
22. Wang, D.; Guo, W.; Zou, Y.; Ma, T.; Wang, W.; Chen, G. Terahertz Refractive Index and Temperature Dual-Parameter Sensor Based on Surface Plasmon Resonance in Two-Channel Photonic Crystal Fiber. *Sensors* **2024**, *24*, 6225. [CrossRef]
23. Saad, N.M.; Rabaie, E.S.M.E. A review of recent developments in photonic crystal fibers (PCFs)-based biomedical and chemical sensing applications. *J. Electr. Syst. Inf. Technol.* **2025**, *12*, 71. [CrossRef]
24. Zhang, R.; Chen, Q.; Liu, K.; Chen, Z.; Li, K.; Zhang, X.; Xu, J.; Pickwell-MacPherson, E. Terahertz microfluidic metamaterial biosensor for sensitive detection of small-volume liquid samples. *IEEE Trans. Terahertz Sci. Technol.* **2019**, *9*, 209–214. [CrossRef]
25. Zhao, Z.; Zhang, R.; Song, H.; Pang, K.; Almaiman, A.; Zhou, H.; Song, H.; Liu, C.; Hu, N.; Su, X.; et al. Modal coupling and crosstalk due to turbulence and divergence on free space THz links using multiple orbital angular momentum beams. *Sci. Rep.* **2021**, *11*, 2110. [CrossRef]
26. He, J.; Wang, J.; Liu, W.; Lu, X.; Lv, J.; Yang, L.; Chu, P.K.; Liu, C. Photonic crystal fiber based on graphene surface plasmon resonance for high-sensitivity terahertz refractive index sensing. *J. Opt. Soc. Am. A* **2024**, *41*, 1279–1286. [CrossRef] [PubMed]
27. Daher, M.G.; Ahmed, A.M.; Armghan, A.; Aldkeelalah, S.S.; Hasanein, M.M.A.; Al-Hmoud, M.; Elsayed, H.A.; Mehaney, A. Novel Discovery of *Giardia lamblia* in Drinking Water Based on Plasmonic Photonic Crystal Fiber Sensor (PCFS). *Plasmonics* **2025**, 1–10. [CrossRef]
28. Sharar, S.S.; Rahad, R.; Haque, M.A.; Sagor, R.H. A numerical investigation of the opposing-face semi circular refractive index sensor for detection of chemical pollutants and heavy metals in water. *Opt. Commun.* **2023**, *549*, 129887. [CrossRef]
29. Sayed, F.A.; Elsayed, H.A.; Al-Dossari, M.; Eissa, M.F.; Mehaney, A.; Aly, A.H. Angular surface plasmon resonance-based sensor with a silver nanocomposite layer for effective water pollution detection. *Sci. Rep.* **2023**, *13*, 21793. [CrossRef]

30. Mortazavi, S.; Makouei, S.; Garamaleki, S.M. Hollow core photonic crystal fiber based carbon monoxide sensor design applicable for hyperbilirubinemia diagnosis. *Opt. Eng.* **2023**, *62*, 066105. [CrossRef]
31. Mohammadi, A.A.; Makouei, S.; Mortazavi, S. Ultra-High Sensitivity and Low Loss: Innovative PCF Simulated Design Featuring I-Holes for Harmful Gas Detection. *Photonics Nanostructures-Fundam. Appl.* **2025**, *66*, 101449. [CrossRef]
32. Pourfathi Fard, A.; Makouei, S.; Danishvar, M.; Danishvar, S. The design of a photonic crystal fiber for hydrogen cyanide gas detection. *Photonics* **2024**, *11*, 178. [CrossRef]
33. Bulbul, A.A.; Hossain, M.B.; Dutta, R.; Hassan, M. Zeonex-based tetra-rectangular core-photonic crystal fiber for NaCl detection. *Nanosci. Nanotechnol.-Asia* **2021**, *11*, 112–120. [CrossRef]
34. Hossain, M.B.; Podder, E.; Bulbul, A.A.M.; Mondal, H.S.; Raihan, M.; Islam, M.T. Identification of cyanide within hollow core photonics crystal fiber. In Proceedings of the 2019 10th International Conference on Computing, Communication and Networking Technologies (ICCCNT), Kanpur, India, 6–8 July 2019; IEEE: New York, NY, USA, 2019; pp. 1–4.
35. Ferdous, A.I.; Hosen, M.S.; Khandakar, K.; Kundu, D.; Bani, M.M.; Noor, K.S.; Tithi, S.A. Pioneering terahertz blood analysis: Hollow-core PCF with optimized sensitivity and low loss. *PLoS ONE* **2025**, *20*, e0319860. [CrossRef]
36. Sen, S.; Abdullah-Al-Shafi, M.; Kabir, M.A. Hexagonal photonic crystal Fiber (H-PCF) based optical sensor with high relative sensitivity and low confinement loss for terahertz (THz) regime. *Sens. Bio-Sens. Res.* **2020**, *30*, 100377. [CrossRef]
37. Habib, A.; Anower, S.; Haque, I. Highly sensitive hollow core spiral fiber for chemical spectroscopic applications. *Sens. Int.* **2020**, *1*, 100011. [CrossRef]
38. Gandhi, M.A.; Zhao, Y.; Fu, H.Y.; Li, Q. A highly versatile porous core photonic quasicrystal fiber based refractive index terahertz sensor. *Sensors* **2022**, *22*, 3469. [CrossRef] [PubMed]
39. Bulbul, A.A.M.; Podder, E.; Ahammad, S.H.; Faragallah, O.S.; Eid, M.M.; Rashed, A.N.Z. Human body cholesterol detection based on a photonic crystal fiber sensor within a hollow octagonal core configuration. *J. Comput. Electron.* **2023**, *22*, 1725–1734. [CrossRef]
40. Faruk, M.O.; Khandakar, K.; Kundu, D.; Ferdous, A.I.; Sonic, M.M.R.; Khan, M.O. Terahertz photonic crystal fiber-based edible oil sensor: Performance evaluation and identification. *Appl. Food Res.* **2024**, *4*, 100537. [CrossRef]